

Great enhancements in the thermoelectric power factor of BiSbTe nanostructured films with well-ordered interfaces†

Cite this: *Nanoscale*, 2013, 5, 7017

Hsiu-Cheng Chang,^a Chun-Hua Chen^{*a} and Yung-Kang Kuo^{*b}

An innovative concept of twin-enhanced thermoelectricity was proposed to fundamentally resolve the high electrical resistance while not degrading the phonon scattering of the thermoelectric nanoassemblies. Under this frame, a variety of highly oriented and twinned bismuth antimony telluride ($\text{Bi}_x\text{Sb}_{2-x}\text{Te}_3$) nanocrystals were successfully fabricated by a large-area pulsed-laser deposition (PLD) technique on insulated silicon substrates at various deposition temperatures. The significant presence of the nonbasal- and basal-plane twins across the hexagonal BiSbTe nanocrystals, which were experimentally and systematically observed for the first time, evidently contributes to the unusually high electrical conductivity of $\sim 2700 \text{ S cm}^{-1}$ and the power factor of $\sim 25 \mu\text{W cm}^{-1} \text{ K}^{-2}$ as well as the relatively low thermal conductivity of $\sim 1.1 \text{ W m}^{-1} \text{ K}^{-1}$ found in these nanostructured films.

Received 26th March 2013
Accepted 27th May 2013

DOI: 10.1039/c3nr01499a

www.rsc.org/nanoscale

Introduction

Nanostructuring, one of the most effective and practical strategies in enhancing the thermoelectric (TE) figure of merit (ZT), not only propels TE materials to the forefront of green power sources but also further accelerates the progress in fundamental research and advanced applications.^{1–3} For realizing the predicted exhilarating ZTs of nanostructures,^{4,5} great research efforts have been initiated and concentrated on preparing quantum crystals from zero to three dimensions and especially their assemblies. In the last decade, numerous novel bismuth telluride (Bi_2Te_3) related bulk or films behind the concept of nanostructuring were extensively investigated to manipulate the size and dimensions as well as the organization of specific nanocrystals. For example, to introduce the spatial confinement, TE nanostructures such as superlattices,⁶ nanostructured bulks,^{7,8} nanoparticles,^{9–11} nanorods,¹² nanowires,¹³ nanoplates,¹⁴ and hierarchical structures^{15,16} have been reported. However, as the sizes or dimensions of the nanoblocks are

steadily reduced, the accompanying interface effects become more significant and cause serious deterioration in the electrical conductivity, even though the thermal conductivity is expected to decrease due to the enhanced phonon scattering.

Reasonably, the key for fundamentally resolving the high interfacial electrical resistance is to alternate the conventional disordered grain boundary with a more perfective one in which phonons are effectively blocked while the scattering of conducting electrons is minimized.^{17,18} A twin boundary, a kind of special coherent grain boundary, is thus considered as one of the candidates with the greatest promise since it has been theoretically and experimentally proven that, with the presence of twin boundaries, the phonons are noticeably scattered^{19–22} but the conducting electrons are not.^{23–25} Zhao *et al.* reported a high ZT value of 1.47 observed in hot-pressed $\text{Bi}_2\text{Te}_3/\text{Sb}_2\text{Te}_3$ nanocomposites in which twin structures constructed the phase boundaries of the alternate Bi_2Te_3 and Sb_2Te_3 nanolayers.²⁶ Obviously, the heterogeneous twins play an important role in obtaining such a high level of electrical conductivity.

In this work, within the frame of nanostructuring, we propose a completely new and intrinsic concept, *i.e.* thermally induced spontaneous growth of highly oriented and twinned nanoassemblies, not only specifically for modifying carrier transport across interfaces, but also for effectively providing extra phonon scattering. This structurally engineered concept was evaluated, designed, realized, and subsequently fully modified based on our exhilarating discoveries from the investigation of highly oriented and twinned bismuth antimony telluride ($\text{Bi}_x\text{Sb}_{2-x}\text{Te}_3$) films and the mentioned instructive reports.^{17–26} Assembling highly oriented nanoblocks can lead to a larger coherent grain size in the out-of-plane direction and the

^aDepartment of Materials Science and Engineering, National Chiao Tung University, Hsin-Chu 30010, Taiwan, ROC. E-mail: ChunHuaChen@mail.nctu.edu.tw

^bDepartment of Physics, National Dong Hwa University, Hua-Lien 97401, Taiwan, ROC. E-mail: ykkuo@mail.ndh.edu.tw

† Electronic supplementary information (ESI) available: Morphologies, XRD patterns, SEM compositions and room-temperature thermoelectric properties of the series of (015) oriented $\text{Bi}_{0.4}\text{Sb}_{1.6}\text{Te}_3$ nanocolumns (Fig. S1–S3), (001) oriented $\text{Bi}_{0.5}\text{Sb}_{1.5}\text{Te}_3$ nanodiscs (Fig. S4–S6), and (001) and (015) doubly oriented $\text{Bi}_{0.5}\text{Sb}_{1.5}\text{Te}_3$ nanodiscs and $\text{Bi}_{0.7}\text{Sb}_{1.3}\text{Te}_3$ nanolayers (Fig. S7–S9). TEM-EDX (Fig. S10), XPS spectra (Fig. S11), HRTEM investigations (Fig. S12–S14), and XRD strain analyses (Fig. S15) of the most outstanding specimens selected from these three series of $\text{Bi}_x\text{Sb}_{2-x}\text{Te}_3$ nanostructures. See DOI: 10.1039/c3nr01499a

formation of small-angle or highly coherent boundaries and interfaces between neighboring nanograins. Significantly high electrical conductivity can thus be expected for such unique nanoassemblies.

To practically approach this innovative concept, a series of twin embedded $\text{Bi}_x\text{Sb}_{2-x}\text{Te}_3$ nanoassemblies have been systematically and successfully prepared *via* an optimized one-step, large-area, non-catalytic and template-free pulsed-laser deposition (PLD) at various deposition temperatures. It is worth emphasizing that the present observed multi-type twin structures formed along or across interfaces between neighboring $\text{Bi}_x\text{Sb}_{2-x}\text{Te}_3$ nanocrystals have not been previously fabricated and reported. We believe that this greatly successful concept as well as the corresponding structural issues and their effects on the thermoelectric properties of $\text{Bi}_x\text{Sb}_{2-x}\text{Te}_3$ nanostructures may fundamentally and simply resolve the high-resistance problems of most nanoassemblies and further lead to a significant breakthrough for thermoelectric nanostructured materials.

Experimental section

Deposition of nanoassemblies

The $\text{Bi}_{0.4}\text{Sb}_{1.6}\text{Te}_3$ powders were dry pressed into discs of 10 mm diameter and 2 mm thickness and were then annealed under a hydrogen atmosphere at 20 torr at 573 K for 10 h. To prevent the substrate effect on the following thermoelectric measurement, a SiO_2 layer with a thickness of 500 nm was thermally grown on the Si substrates. The crystal structure and composition of the prepared targets for PLD were confirmed as those of the starting powders. A Q-switched Nd:YAG pulsed laser (Litron, LPY 664) with a focused laser fluence of about 8.3 J cm^{-2} (355 nm wavelength, 10 ns pulse duration, 8 mm beam diameter and 5 Hz repetition rate) was kept for the deposition processes. The deposition chamber was evacuated to a base pressure of 5×10^{-6} torr and 99.999% purity Ar was then introduced for the pressure control at various substrate temperatures from 673 K to 883 K.

Structural characterizations

The morphology and film thickness of the $\text{Bi}_x\text{Sb}_{2-x}\text{Te}_3$ nanostructured films were examined by field emission scanning electron microscopy (FE-SEM, JEOL JSM-6500). The preferential orientation and crystallinity of the prepared $\text{Bi}_x\text{Sb}_{2-x}\text{Te}_3$ nanoassemblies were determined by X-ray diffraction (XRD, Bruker AXS, D8 Discover) with Cu K α radiation ($\lambda = 1.54 \text{ \AA}$). All the XRD patterns were recorded in a θ - 2θ configuration and carefully calibrated by their own Si(100) substrates. TEM images were obtained using transmission electron microscopy (TEM, JEOL JEM-3000F) with energy dispersive spectroscopy (EDS, Oxford). The oxidation of each component in $\text{Bi}_x\text{Sb}_{2-x}\text{Te}_3$ was characterized by X-ray photoelectron microscopy (XPS, Thermo VG 350). All the recorded spectra were corrected by external Pt signals to prevent the charge effect.

Thermoelectric properties

The carrier concentration and mobility of the $\text{Bi}_x\text{Sb}_{2-x}\text{Te}_3$ nanostructured films were measured by a Hall system (Accent

HL5500) with van der Pauw methods at room temperature. The in-plane electrical resistivity and Seebeck coefficient were obtained in a closed-cycle refrigerator over temperatures from 10 to 300 K, respectively using a standard dc four-terminal method and a direct heat-pulse technique. The samples for Seebeck coefficient measurement were cut to a typical size of $1.5 \times 5.0 \text{ mm}^2$, with one end glued (with thermal epoxy) to a copper block as a heat sink. A chip resistor (RuO, provided by Mini Systems, Inc.) with a room-temperature resistance of 100 ohm ($\pm 0.5\%$) was used to generate temperature gradient for the Seebeck coefficient measurements. The temperature-dependent resistance of the chip resistor was carefully calibrated in the temperature range of 4 to 400 K by a semi-four probe method. With known resistance and applied current to the chip resistor, the power input to the measured samples is therefore obtained and the temperature gradient can be precisely controlled during the Seebeck coefficient measurements while varying temperature. The temperature difference was controlled to be about 1 K. During measurements, the sample space was maintained in a good vacuum (better than 10^{-4} torr). Seebeck voltages were detected using a pair of thin Cu wires electrically connected to the sample with silver paint at the same positions as the junctions of a differential thermocouple. The stray thermal emfs (electromotive forces) were eliminated by applying long current pulses (~ 100 s) to the chip resistor, where the pulses appeared in an off-on-off sequence. All experiments were performed on warming at a rate slower than 20 K h^{-1} . The reproducibility of Seebeck measurements is better than 2%. The details of the measurement techniques can be found elsewhere.^{27,28} The cross-plane thermal conductivity of the $\text{Bi}_x\text{Sb}_{2-x}\text{Te}_3$ nanoassemblies was measured using a well-developed 3ω technique.²⁹ A $\text{SiO}_2/\text{Bi}_x\text{Sb}_{2-x}\text{Te}_3/\text{SiO}_2$ sandwiched film structure was especially deposited for this measurement where the thickness of the sputtered SiO_2 was 100 nm. The patterned Au/Cr electrodes prepared by a microlithography process on the top SiO_2 surface served as a heater and a thermometer as well. To extract the intrinsic thermal conductivity of the $\text{Bi}_x\text{Sb}_{2-x}\text{Te}_3$ nanoassemblies, the thermal resistances of the SiO_2 films and the various interfaces of the sandwiched structure have to be excluded. The thickness-dependent cross-plane thermal conductivity (κ) and the thermal resistance (R_{th}) are represented by³⁰

$$\kappa = \frac{\kappa_i}{1 + \kappa_i R_i / d_f} \quad (1)$$

and

$$R_{\text{th}} = \frac{d_f}{\kappa} = R_i + \frac{d_f}{\kappa_i} \quad (2)$$

respectively, where κ_i is the intrinsic thermal conductivity of the $\text{Bi}_x\text{Sb}_{2-x}\text{Te}_3$ layer, which is assumed to be a constant and to be thickness-independent, d_f the thickness of the $\text{Bi}_x\text{Sb}_{2-x}\text{Te}_3$ layer, and R_i the total interface thermal resistance from metal strips to the substrate. The R_i and κ_i can thus be respectively determined from the plot of R_{th} versus d_f . The measurement was performed at 300 K in a vacuum chamber (10^{-3} torr).

Results and discussion

As addressed above, twin interfaces might be some of the mostly appreciated structures not only for significantly lowering the electrical resistance, but for acquiring desired thermal conductivity. A practical method for effectively forming twin structures in thermoelectric nanomaterials is thus very critical to realize this twin concept. Fig. 1 shows the SEM observations of a series of $\text{Bi}_{0.5}\text{Sb}_{1.5}\text{Te}_3$ nanostructured films deposited at 773, 823, and 873 K under an Ar ambient pressure of 0.15 torr for 3 h. According to their disc-like morphologies (see Fig. 1a–c), these films were named as nanodiscs. The cross-sectional images (Fig. 1d–f) show that the continuity and regularity of the stacks of discs is slightly improved as the deposition temperature increases. From the XRD patterns displayed in Fig. 2a, an obvious (001) basal-plane preferential orientation can also be found for all these specimens. Such epitaxy-like morphology and highly preferential orientation are geometrically beneficial for forming coherent grain boundaries, *e.g.* twins or small-angle grain boundaries, as will be proven in the following high-resolution TEM (HRTEM) analyses. More than the successfully controlled structures, SEM-EDS measurement shown in Fig. 2b confirms that these nanodiscs have a very close chemical composition of $\text{Bi} : \text{Sb} : \text{Te} = 10 : 30 : 60$.

Fig. 3 shows the TEM analysis of the specimen deposited at 773 K for further understanding the details of the film quality,

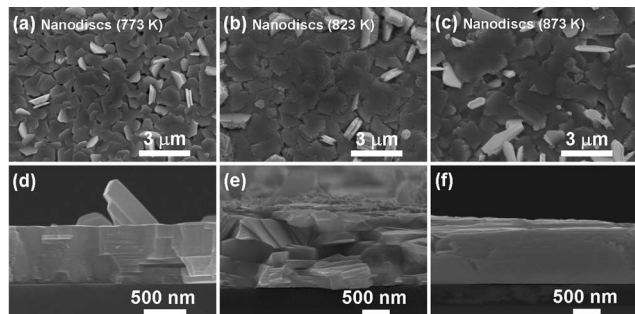


Fig. 1 Top-view SEM images of nanodiscs deposited at (a) 773 K, (b) 823 K, and (c) 873 K. The corresponding cross-sectional SEM images are shown along with (a)–(c).

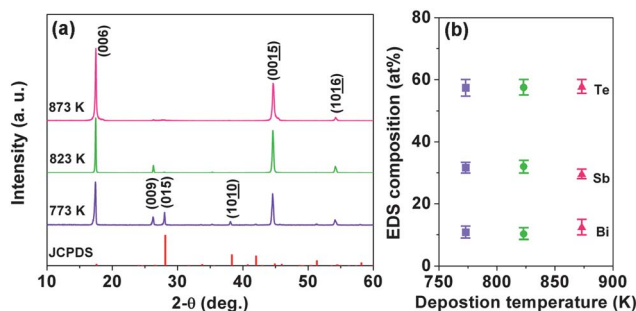


Fig. 2 (a) X-ray diffraction patterns recorded from the (001) oriented $\text{Bi}_{0.5}\text{Sb}_{1.5}\text{Te}_3$ nanodiscs prepared at 773, 823, and 873 K. (b) The SEM-EDS compositions as a function of the deposition temperature.

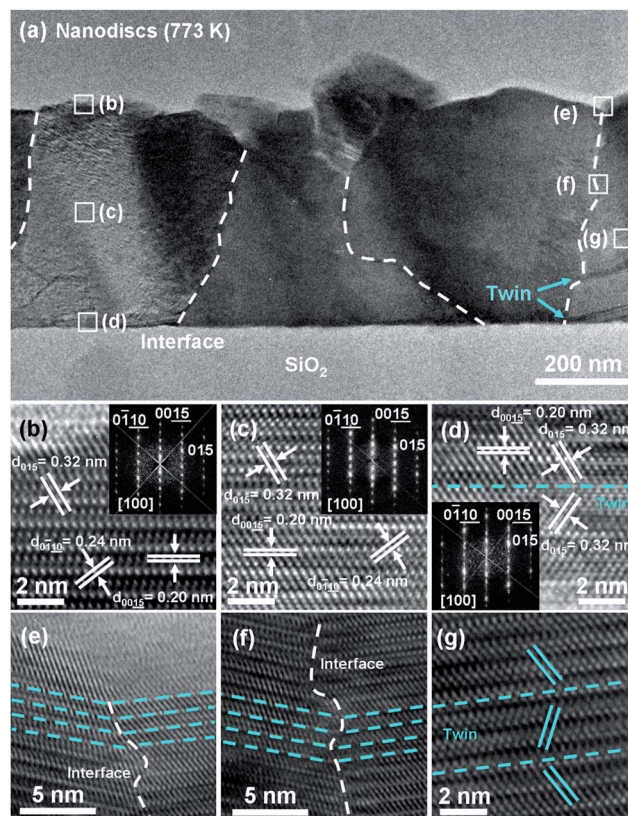


Fig. 3 (a) Cross-sectional TEM image of the $\text{Bi}_{0.5}\text{Sb}_{1.5}\text{Te}_3$ nanodiscs deposited on SiO_2/Si substrates at 773 K showing a uniform film thickness of ~ 690 nm and obvious interfaces as indexed by dashed lines. (b–d) The selected regions for HRTEM imaging and the corresponding FFT ED patterns. The zone axis and a few main reciprocal lattice points are indexed. The HRTEM images of (e and f) twin boundaries between neighboring grains and (g) the basal-plane twin band.

especially the grain boundary conditions. As denoted in Fig. 3a, different regions within one domain and across neighboring domains separated by dashed lines were selected for HRTEM analyses. From the lattice fringes as well as the vertically dense FFT ED spots shown in Fig. 3b–d, numerous twins parallel to the basal planes are evidently found in the whole grain. The slightly elongated diffraction spots suggest the presence of a small misorientation deviating from the perfect alignment between the nanocrystallines in the resulting nanodiscs. The clear interface along two neighboring grains as shown in Fig. 3e and f obviously indicates a nonbasal-plane twin boundary. The lattice planes smoothly move from the right-side to the left-side grain, indicating that the twin boundary has a rather high coherent degree. In region (f), the mismatches between lattice planes across these two domains as indexed evidence a defective twin boundary. We believe that such nonbasal-plane twin boundaries formed between neighboring grains having similar orientations can provide large-area pathways for electron transport and lead to a high electrical conductivity as will be discussed below. In addition, a clear pair of the basal-plane twin boundary was found to form a twin band having a band width of ~ 3 nm (Fig. 3g), which is comparable to the lattice constant c of the hexagonal $\text{Bi}_x\text{Sb}_{2-x}\text{Te}_3$. The TEM image (Fig. 3a) showing

densely appeared twin bands parallel to the (001) oriented grains around the (g) region evidently proves the twins across whole grains to reach the twin boundaries. It is worth emphasizing that the great presence of the twin networks within the prepared (001) oriented $\text{Bi}_{0.5}\text{Sb}_{1.5}\text{Te}_3$ nanodiscs directly contributes the observed remarkably high in-plane electrical conductivity of $\sim 1000 \text{ S cm}^{-1}$, which is much higher than most intrinsic and doped Bi_2Te_3 nanostructured films that have been reported to date (see Table 1). In addition to the (001) oriented $\text{Bi}_{0.5}\text{Sb}_{1.5}\text{Te}_3$ nanodiscs, we also systematically and successfully prepared a set of (015) oriented $\text{Bi}_{0.4}\text{Sb}_{1.6}\text{Te}_3$ nanocolumns and a set of (015) and (001) doubly oriented $\text{Bi}_{0.3}\text{Sb}_{1.7}\text{Te}_3$ nanolayers and carried out similar investigations as can be found in the ESI (see Fig. S1–S9†).

The most outstanding specimens selected from these three types of oriented $\text{Bi}_x\text{Sb}_{2-x}\text{Te}_3$ nanostructures were collected and compared for fundamental understanding of the distinct features of the twins found in these three very different nanostructures, as well as the resulting thermoelectric properties. Fig. 4 shows the SEM images of the most commonly featured $\text{Bi}_x\text{Sb}_{2-x}\text{Te}_3$ nanostructures including nanocolumns, nanodiscs, and nanolayers deposited at 673, 773, and 883 K, respectively. For identifying the preferential orientation normal to the substrate surface, the XRD patterns, together with a reference of rhombohedral $\text{Bi}_{0.4}\text{Sb}_{1.6}\text{Te}_3$ (JCPDS 65-3674), are shown in Fig. 5a. The absence of Bi_2Te_3 and Sb_2Te_3 phases, and traceable impurities such as metallic Te as frequently found in physical depositions, indicates that the specimens were well alloyed. Quantitatively analyzing the integrated intensity of reflections, significant (015), (001), and a double orientation of (015) and (001) are observed for specimens prepared at 673, 773, and 883 K, respectively. The lattice constants obtained from the full pattern refinements of the hexagonal $\text{Bi}_x\text{Sb}_{2-x}\text{Te}_3$ are shown in Fig. 5b. Since the covalent radius of Sb (1.40 Å) is smaller than

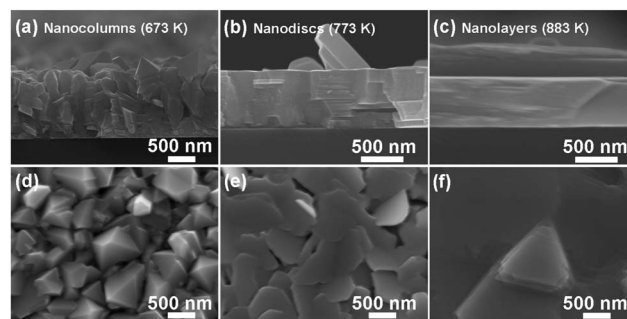


Fig. 4 (a–c) Cross-sectional SEM images of self-assembled $\text{Bi}_x\text{Sb}_{2-x}\text{Te}_3$ nanocolumns, nanodiscs, and nanolayers deposited on SiO_2/Si substrates at 673, 773, and 883 K, respectively. The corresponding top-view SEM images are shown in (d)–(f).

that of Bi (1.46 Å),³¹ the approximate linear change of the lattice constants with deposition temperature indicates an accompanying variation of the Sb/Bi substitution ratio under the present deposition conditions. The EDS analysis acquired from SEM (Fig. 5c) and TEM (Fig. S10†) confirmed that the composition of the nanoassemblies at 673, 773, and 883 K can be optimized as $\text{Bi}_{0.4}\text{Sb}_{1.6}\text{Te}_3$, $\text{Bi}_{0.5}\text{Sb}_{1.5}\text{Te}_3$, and $\text{Bi}_{0.7}\text{Sb}_{1.3}\text{Te}_3$, respectively. The XPS measurements (Fig. S11†) suggest that the surfaces of the prepared films are oxide free.

We have previously proven that the morphologies of the Bi_2Te_3 nanostructures prepared by the present PLD system can be predicted by the well-known structure zone model (SZM).^{32,33} Regarding the preferential orientations found in this work, it is much easier to understand their formation mechanisms by replacing the large and completed hexagonal unit cell with much smaller and simpler pseudo face-center-cubic (fcc) ones as plotted in Fig. 5d, where the hexagonal (015) and (001) can be alternated with pseudo-(100) and pseudo-(111) in fcc,

Table 1 Progress of some related Bi_2Te_3 -based nanostructured films and bulks. All the selected values were recorded at room temperature

System	Type	n (10^{19} cm^{-3})	μ ($\text{cm}^2 \text{ V}^{-1} \text{ s}^{-1}$)	σ (S cm^{-1})	S ($\mu\text{V K}^{-1}$)	$S^2\sigma$ ($\mu\text{W cm}^{-1} \text{ K}^{-2}$)	κ ($\text{W m}^{-1} \text{ K}^{-1}$)	ZT	Ref.
Bi_2Te_3	Bulk	—	—	49.6	−91	0.41	0.51	0.02	9
	Bulk	—	—	769	−80	4.92	—	—	10
	Bulk	—	—	5	−172	0.148	0.3	0.016	15
	Film	—	—	—	−107	—	—	—	11
	Film	—	—	6	−100	0.06	—	—	12
	Film	—	—	23.15	−150	0.52	—	—	13
	Film	—	—	0.4	−131	0.007	—	—	14
$\text{Bi}_{0.4}\text{Sb}_{1.6}\text{Te}_3$	Single crystal	4.8	176	1000	194	37.6	1.3	0.87	31
	Bulk	2.2	178	617	204	25.7	0.85	0.91	48
	Bulk	1.7	136	370	216	17.3	0.67	0.78	48
	Bulk	—	—	275	153	6.4	0.40	0.5	49
$\text{Bi}_{0.5}\text{Sb}_{1.5}\text{Te}_3$	Single crystal	3.5	177	769	225	38.9	1.4	0.84	31
	Bulk	2.5	264	1280	185	43.7	1.1	1.10	7
	Bulk	3.4	210	1250	200	50.0	1.1	1.36	8
	Bulk	1.4	49	110	257	7.2	—	—	45
	Film	2	73	208	205	8.7	0.7	—	50
$(\text{Bi}_{0.5}\text{Sb}_{0.5})_2\text{Te}_3$	Film	—	—	410	215	19	—	—	51
$\text{Bi}_{0.7}\text{Sb}_{1.3}\text{Te}_3$	Single crystal	6	200	2000	120	28.8	1.6	0.54	52
	Film	15	23.8	560	135	10.2	1.1	0.28	46
$\text{Bi}_{0.1}\text{Sb}_{1.9}\text{Te}_3$	Film	27.4	12	526	164	14.1	—	—	47

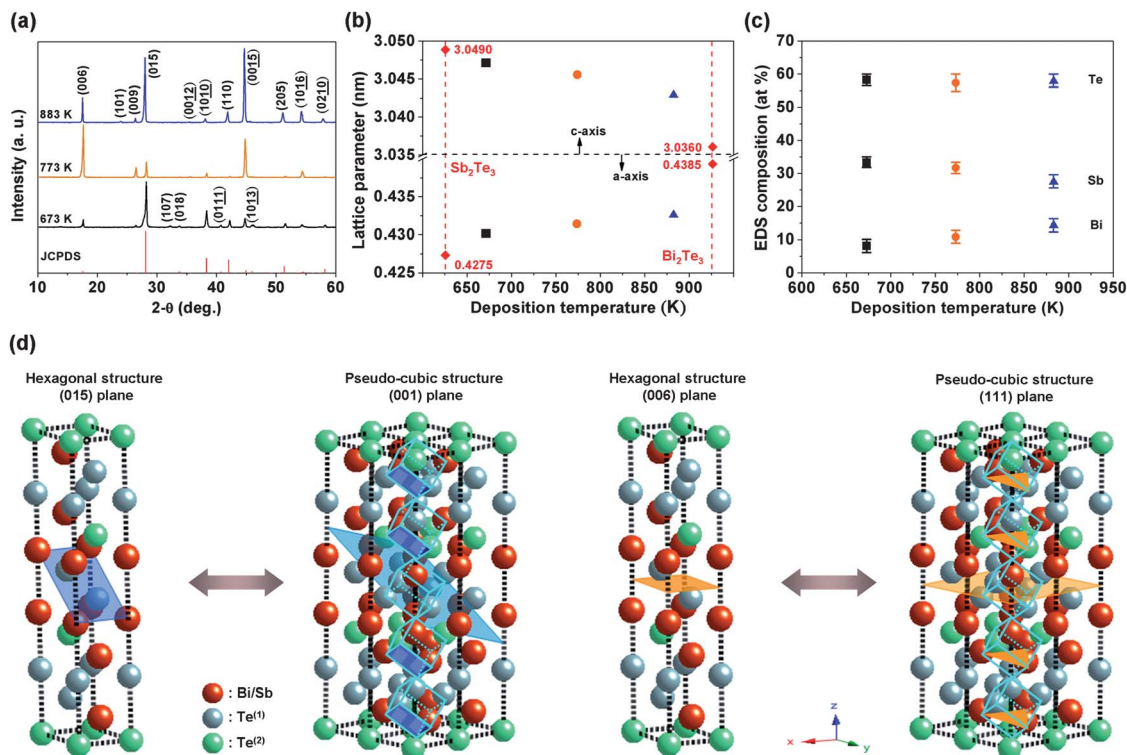


Fig. 5 (a) The θ - 2θ XRD patterns and (b) the corresponding refined lattice parameters of hexagonal c and a , obtained from the prepared distinct $\text{Bi}_x\text{Sb}_{2-x}\text{Te}_3$ nanoassemblies deposited at 673 (squares), 773 (circles), and 883 K (triangles), respectively. The lattice parameters of Sb_2Te_3 (JCPDS 065-3678) and Bi_2Te_3 (JCPDS 089-4302) are also represented for comparison purposes (diamonds). (c) The atomic ratios of Bi, Sb, and Te components are determined by EDX as functions of deposition temperatures. The stoichiometric composition is found as $\text{Bi}_{0.4}\text{Sb}_{1.6}\text{Te}_3$ (673 K), $\text{Bi}_{0.5}\text{Sb}_{1.5}\text{Te}_3$ (773 K), and $\text{Bi}_{0.7}\text{Sb}_{1.3}\text{Te}_3$ (883 K). (d) Schematic illustration of the geometric relationship between the hexagonal $(\text{Bi/Sb})_2\text{Te}_3$ unit cell and the pseudo-cubic ones. The hexagonal (015) and (001) can be alternated with the pseudo-cubic (100) and (111), respectively.

respectively.^{34,35} For fcc structures, the order of the three low-index surface energies is $E^S_{(111)} < E^S_{(100)} < E^S_{(110)}$.³⁶ When the ablated clusters or plasma species arrived at heated substrates, atoms tend to form new surfaces with lower surface energies to reduce the total energies. However, whether the lowest-energy surface can be formed, *i.e.* (111) in fcc, depends strongly on whether the deposition temperature is high enough to provide the diffusion energy of the atoms deposited. Bassi *et al.* also experimentally showed that hexagonal Bi_2Te_3 (001) tends to appear at higher deposition temperatures (>620 K), otherwise the (015) phase would form.^{37,38}

HRTEM observations were performed to investigate the oriented and twinned $\text{Bi}_x\text{Sb}_{2-x}\text{Te}_3$ nanocrystals. Fig. 6a–c, showing the twin structures across whole grains of the present assembled films, confirm that we have successively implanted twin structures in oriented $\text{Bi}_{0.4}\text{Sb}_{1.6}\text{Te}_3$ nanocolumns, $\text{Bi}_{0.5}\text{Sb}_{1.5}\text{Te}_3$ nanodiscs, and $\text{Bi}_{0.7}\text{Sb}_{1.3}\text{Te}_3$ nanolayers at 673, 773, and 883 K, respectively. The clear interface along two neighboring grains, as shown in Fig. 6d–f, obviously indicates a nonbasal-plane twin boundary. The lattice planes smoothly move from the left-side to the right-side grain, indicating that the twin boundary has a rather high coherent degree. We believe that such nonbasal-plane twin boundaries formed between neighboring grains having similar orientations can provide large-area pathways for electron transport and lead to a

high electrical conductivity. In addition, a clear mirror symmetrical lattice plane was found in Fig. 6g–i, indicating the existence of basal-plane twin structures parallel to the substrate, which is comparable to the lattice constant c of the hexagonal $\text{Bi}_x\text{Sb}_{2-x}\text{Te}_3$. The formation of twinned crystals is kinetically driven, and the nucleation and growth rate of twinned crystals are controlled by the deposition conditions. To alternate defective high-angle grain boundaries for reducing total energy, twinned structures are thus preferred to nucleate at grain boundaries or triple junctions by means of the twinning-induced orientation change.^{23,39} Higher deposition temperature is thus helpful to provide excess energy to increase the nucleation rate of twins at grain boundaries and triple junctions. Medlin *et al.* have estimated interfacial energies of basal-plane twin planes terminated at different atomic layers, and found that the interfacial energy calculated is in the order of $\text{Bi} > \text{Te}^{(2)} > \text{Te}^{(1)}$.⁴⁰ Precisely comparing the simulated lattice fringes of twin planes located at these three layers,⁴⁰ we found that the twinned structures observed in $\text{Bi}_{0.4}\text{Sb}_{1.6}\text{Te}_3$ nanocolumns (673 K), $\text{Bi}_{0.5}\text{Sb}_{1.5}\text{Te}_3$ nanodiscs (773 K), and $\text{Bi}_{0.7}\text{Sb}_{1.3}\text{Te}_3$ nanolayers (883 K) are terminated at the Bi/Sb, $\text{Te}^{(2)}$, and $\text{Te}^{(1)}$ layers, respectively (see Fig. 6g–i). The present results obviously indicate a strong correlation between the formation of twins and the deposition temperature applied; that is, a higher deposition temperature tends to form twins with lower

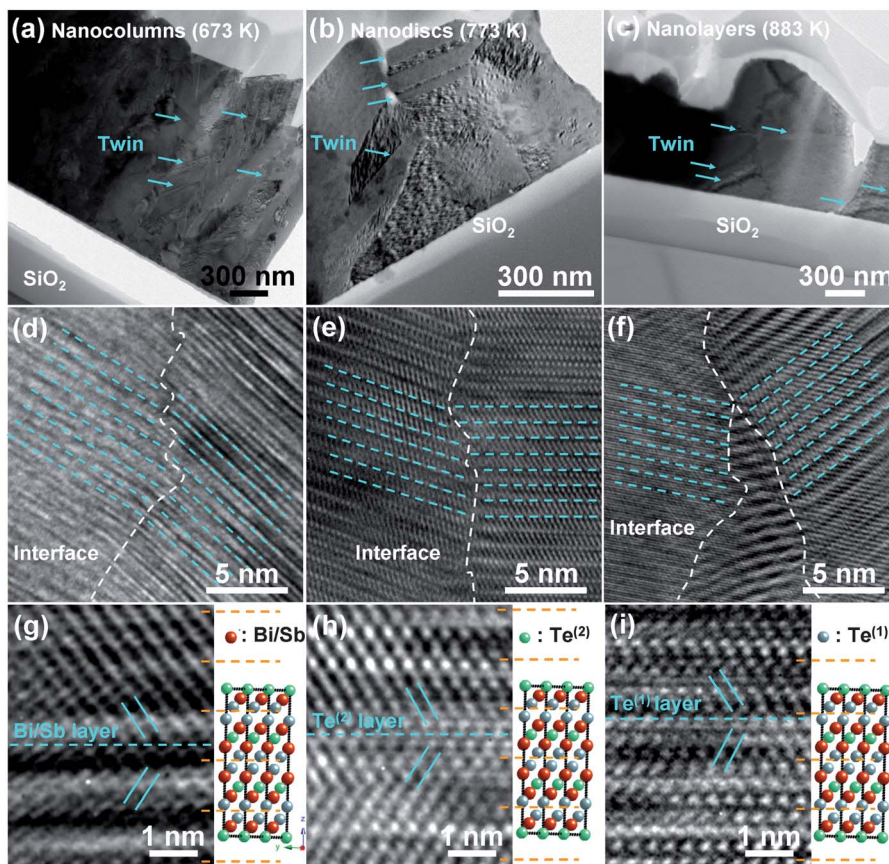


Fig. 6 The cross-sectional TEM images of the (a) $\text{Bi}_{0.4}\text{Sb}_{1.6}\text{Te}_3$ nanocolumns, (b) $\text{Bi}_{0.5}\text{Sb}_{1.5}\text{Te}_3$ nanodiscs, and (c) $\text{Bi}_{0.7}\text{Sb}_{1.3}\text{Te}_3$ nanolayers, respectively, obtained at 673, 773, and 883 K show significant twin structures through the whole grain. The HRTEM images of the nonbasal-plane twin boundaries found between neighboring grains are displayed in (d)–(f). The basal-plane twins terminated at Bi/Sb, $\text{Te}^{(2)}$, and $\text{Te}^{(1)}$ atomic layers are clearly shown in (g)–(i), respectively.

interfacial energy. In addition, it seems that 673 K is not high enough to form non-basal and basal-plane twin planes with high qualities due to the unclear twin fringes as shown in Fig. 6d and g. The detailed HRTEM investigations (Fig. S12–S14†) and XRD strain analyses (Fig. S15†) are shown in the ESI.†

Fig. 7 shows the most important characteristics in this article: a series of remarkable temperature-dependent thermoelectric properties measured along the in-plane direction. The positive Hall coefficients indicate that the holes are the major carriers for all the prepared $\text{Bi}_x\text{Sb}_{2-x}\text{Te}_3$ nanostructures. The nanolayers intriguingly exhibit a much higher carrier concentration ($\sim 2.4 \times 10^{20} \text{ cm}^{-3}$) than nanocolumns ($\sim 1.3 \times 10^{19} \text{ cm}^{-3}$) and nanodiscs ($\sim 2.9 \times 10^{19} \text{ cm}^{-3}$), as displayed in Fig. 7a. At higher temperatures, due to the much higher volatilization rate of the tellurium element (vapor pressure: $\text{Te} > \text{Sb} > \text{Bi}$),⁴¹ the Te vacancy (V_{Te}) would significantly form, as frequently observed in previous reports.⁴² The smaller difference in electronegativity between Bi and Te atoms is considered to drive the Bi atoms to occupy the created Te vacancies.⁴³ Accompanying the generation of the antisite defects (Bi_{Te}) and Bi vacancies (V_{Bi}), the unbalanced charge is respectively compensated by one and three holes.⁴⁴ As the deposition temperature increases, the volatilization of the Te component becomes more severe and thus the carrier concentration

simultaneously increases. These obtained carrier concentrations are consistent with those previously reported (10^{19} to 10^{21} cm^{-3})⁴⁵ and correspond well to their compositions as described in Fig. 5b–c. On the other hand, even though the estimated carrier mobility of the nanolayers ($69.5 \text{ cm}^2 \text{ V}^{-1} \text{ s}^{-1}$) is lower than that of both the nanocolumns ($153 \text{ cm}^2 \text{ V}^{-1} \text{ s}^{-1}$) and the nanodiscs ($203 \text{ cm}^2 \text{ V}^{-1} \text{ s}^{-1}$), it is still 2–4 times higher than that of the nanostructured films with a similar hole concentration $\sim 10^{20} \text{ cm}^{-3}$ (ref. 46 and 47) (see Table 1). It is worth noting that both of the nanocolumns and nanodiscs show comparable mobilities with those of the $\text{Bi}_{0.4}\text{Sb}_{1.6}\text{Te}_3$ and $\text{Bi}_{0.5}\text{Sb}_{1.5}\text{Te}_3$ single crystals³¹ indicating that the non-basal plane twins promote the carrier transport in the in-plane direction.

According to the temperature-dependent electrical conductivity $\sigma(T)$ shown in Fig. 7b, the present $\text{Bi}_x\text{Sb}_{2-x}\text{Te}_3$ nanostructures exhibit typical metallic behavior, as the electrical conductivity increases with decreasing temperature in the temperature range investigated (10–300 K). It is worth mentioning that the present room-temperature electrical conductivities of both $\text{Bi}_{0.7}\text{Sb}_{1.3}\text{Te}_3$ nanolayers (2700 S cm^{-1}) and $\text{Bi}_{0.5}\text{Sb}_{1.5}\text{Te}_3$ nanodiscs (1100 S cm^{-1}) are up to three orders of magnitude higher than those of Bi_2Te_3 ($1–500 \text{ S cm}^{-1}$)^{9–15} and $\text{Bi}_x\text{Sb}_{2-x}\text{Te}_3$ ($100–1200 \text{ S cm}^{-1}$)^{7,8,45–51} nanostructured films and

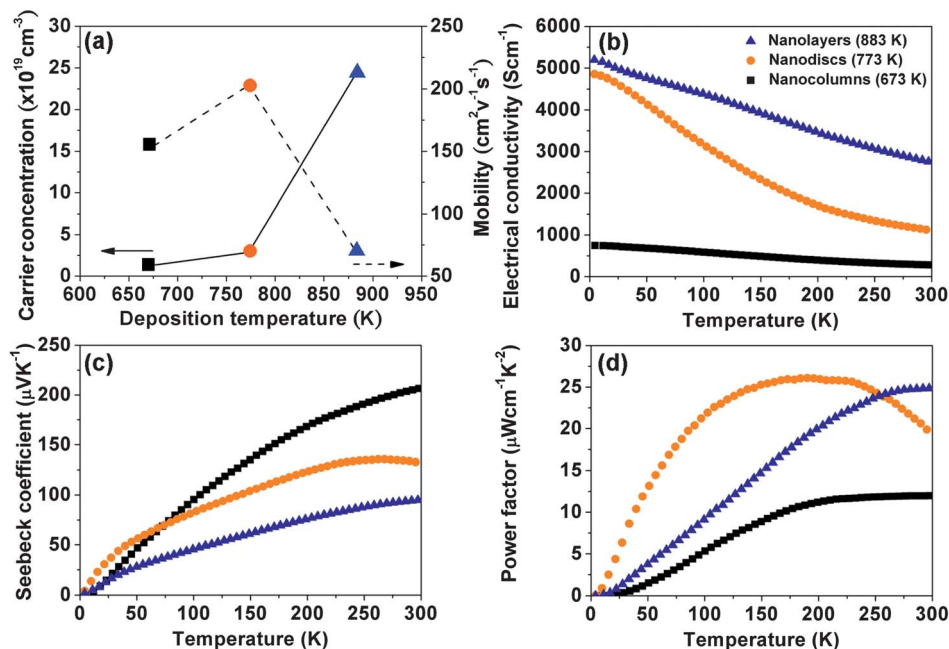


Fig. 7 In-plane thermoelectric properties of $\text{Bi}_{0.4}\text{Sb}_{1.6}\text{Te}_3$ (673 K), $\text{Bi}_{0.5}\text{Sb}_{1.5}\text{Te}_3$ (773 K), and $\text{Bi}_{0.7}\text{Sb}_{1.3}\text{Te}_3$ (883 K) nanoassemblies: (a) the carrier concentration (solid line) and mobility (dashed line) measured at room temperature. (b) The electrical resistivity, (c) Seebeck coefficient, and (d) power factor as functions of temperature.

bulks that have been reported to date (see Table 1). Particularly, the optimized value obtained from the nanolayers is comparable with the level of single-crystalline bulk with a similar stoichiometry ($\sim 2000 \text{ S cm}^{-1}$ for $\text{Bi}_{0.7}\text{Sb}_{1.3}\text{Te}_3$ (ref. 52)). Such a finding can be considered among the most promising advances in the field of Bi_2Te_3 -based thermoelectric nanoassemblies.

Fig. 7c presents the Seebeck coefficient $S(T)$ of $\text{Bi}_x\text{Sb}_{2-x}\text{Te}_3$ nanostructures as a function of temperature. The positive sign of all measured Seebeck coefficients is in agreement with the Hall measurements and indicates that the hole-type carriers dominate the thermoelectric transport in the whole temperature range. The Seebeck coefficients of the nanocolumns and nanolayers increase with increasing temperature and then respectively reach maximum values of $207 \mu\text{V K}^{-1}$ and $95 \mu\text{V K}^{-1}$ at 300 K. In the case of nanodiscs, the Seebeck coefficient reaches a maximum value of $136 \mu\text{V K}^{-1}$ at 264 K and then slightly decreases to $132 \mu\text{V K}^{-1}$ at 300 K. The present nanocolumns show a much more enhanced value of S than that of nanostructured $\text{Bi}_{0.4}\text{Sb}_{1.6}\text{Te}_3$ bulk⁴⁹ whereas the S values of nanodiscs and nanolayers are slightly lower than those reported with similar compositions, most likely due to their considerably high electrical conductivities. It is noted that the S for nanolayers is close to the value reported for a single crystal.⁵² Fig. 7d shows the temperature-dependent power factor of the three prepared $\text{Bi}_x\text{Sb}_{2-x}\text{Te}_3$ nanostructures. The much higher power factors of both nanodiscs and nanolayers are a consequence of their extremely high electrical conductivity, even though their Seebeck coefficients are moderate. Since the power factors of these $\text{Bi}_x\text{Sb}_{2-x}\text{Te}_3$ nanostructures show either downturn or saturation at high temperatures, we thus estimate that the values of maximum power factor are about $26 \mu\text{W cm}^{-1} \text{K}^{-2}$ (at 185 K), $25 \mu\text{W cm}^{-1} \text{K}^{-2}$ and $12 \mu\text{W cm}^{-1} \text{K}^{-2}$ (at room temperature) for

nanodiscs, nanolayers and nanocolumns, respectively. It is worth noting that the maximum power factor obtained from the $\text{Bi}_{0.7}\text{Sb}_{1.3}\text{Te}_3$ nanolayer is higher than most of the nanostructured BiSbTe films^{46,47,50,51} and closely approaches the $\text{Bi}_{0.7}\text{Sb}_{1.3}\text{Te}_3$ single crystal ($28.8 \mu\text{W cm}^{-1} \text{K}^{-2}$).⁵² Thus, it seems reasonable to consider that the highly oriented grains with non-oxidized interfaces in both nanolayers and nanodiscs play a crucial role in the high electrical conductivity as well as the corresponding high power factor. Based on the above results, strong correlations between the preferential orientation, the twin structures, and the extremely high electrical conductivity of the $\text{Bi}_{0.7}\text{Sb}_{1.3}\text{Te}_3$ nanolayers are realized.

The 3ω analysis was applied to examine the cross-plane thermal conductivity of the prepared $\text{Bi}_x\text{Sb}_{2-x}\text{Te}_3$ nanoassemblies at room temperature. As can be seen in Fig. 8, there is a perfect linear relationship between the measured cross-plane thermal resistance and the $\text{Bi}_x\text{Sb}_{2-x}\text{Te}_3$ film thickness. The inset depicts the sandwiched structure used for this technique. The estimated intrinsic thermal conductivity of the $\text{Bi}_x\text{Sb}_{2-x}\text{Te}_3$ nanolayers, nanodiscs, and nanocolumns is 1.16, 1.00, and $0.93 \text{ W m}^{-1} \text{K}^{-1}$, respectively. Obviously, the films with smaller grains and more defective or porous structures exhibit lower thermal conductivities. Considering the thickness effect, the cross-plane thermal conductivity of the nanolayers, nanodiscs, and nanocolumns is $1.10 \text{ W m}^{-1} \text{K}^{-1}$ (490 nm), $0.97 \text{ W m}^{-1} \text{K}^{-1}$ (690 nm), and $1.00 \text{ W m}^{-1} \text{K}^{-1}$ (1250 nm), respectively. These values are very close to that of the nanostructured bulk with similar compositions (see Table 1), indicating that the multiple basal twins embedded in the nanocrystals (see Fig. S12–S15[†]) should effectively lead to phonon scattering while phonons are transported along the cross-plane direction. The valuable experimental evidence

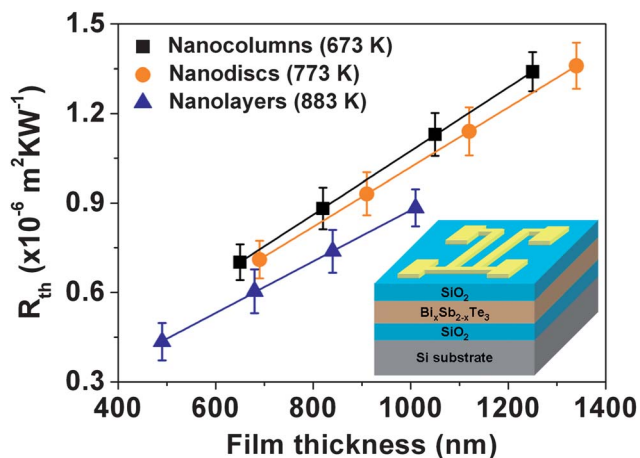


Fig. 8 The total thermal resistance of the $\text{Bi}_x\text{Sb}_{2-x}\text{Te}_3$ nanoassemblies deposited at 673, 773, and 883 K as a function of film thickness. The inset is the sandwiched film structure for the 3ω measurement.

suggests that the partial coherent nonbasal-plane twin boundaries and the dense basal-plane coherent twin bands may become the most potential and desirable interfaces for thermoelectric applications because their highly ordered atomic arrangement could be advantageous for electrical transport while providing additional channels for phonon scattering.

Conclusions

A variety of distinct $\text{Bi}_x\text{Sb}_{2-x}\text{Te}_3$ nanoassemblies, including the (015) and (001) double oriented nanolayers, (001) oriented nanodiscs, and (015) oriented nanocolumns have been successfully fabricated by PLD at various ambient pressures and deposition temperatures from 673 K to 883 K. The existence of two types of twinned structures, the nonbasal-plane twin boundaries and the basal-plane twin bands across the whole grains, as directly shown by HRTEM images, not only provides highly coherent and low-resistance interfaces for smoothly mediating electrons to have a markedly high electrical conductivity as observed in the $\text{Bi}_{0.7}\text{Sb}_{1.3}\text{Te}_3$ nanolayers, but may also act as effective interfaces for phonon scattering. The present highly oriented and twinned crystals stimulate new scientific inquiries and ideas on designing more efficient thermoelectric nanomaterials, thereby circumventing and paving the way for applications in thermoelectric devices.

Acknowledgements

Financial support from the National Science Council of the Republic of China under grant NSC-100-2221-E-009-056, NSC-100-2622-E-009-009-CC2, and NSC-101-2221-E-009-045-MY2 is gratefully acknowledged.

Notes and references

1 M. S. Dresselhaus, G. Chen, M. Y. Tang, R. Yang, H. Lee, D. Wang, Z. Ren, J.-P. Fleurial and P. Gogna, *Adv. Mater.*, 2007, **19**, 1043.

- 2 C. J. Vineis, A. Shakouri, A. Majumdar and M. G. Kanatzidis, *Adv. Mater.*, 2010, **22**, 3970.
- 3 Y. Lan, A. J. Minnich, G. Chen and Z. Ren, *Adv. Funct. Mater.*, 2010, **20**, 357.
- 4 L. D. Hicks and M. S. Dresselhaus, *Phys. Rev. B: Condens. Matter Mater. Phys.*, 1993, **47**, 12727.
- 5 L. D. Hicks and M. S. Dresselhaus, *Phys. Rev. B: Condens. Matter Mater. Phys.*, 1993, **47**, 16631.
- 6 R. Venkatasubramanian, E. Siivola, T. Colpitts and B. O'Quinn, *Nature*, 2001, **413**, 597.
- 7 B. Poudel, Q. Hao, Y. Ma, Y. Lan, A. Minnich, B. Yu, X. Yan, D. Wang, A. Muto, D. Vashaee, X. Chen, J. Liu, M. S. Dresselhaus, G. Chen and Z. Ren, *Science*, 2008, **320**, 634.
- 8 W. Xie, J. He, H. J. Kang, X. Tang, S. Zhu, M. Laver, S. Wang, J. R. D. Copley, C. M. Brown, Q. Zhang and T. M. Tritt, *Nano Lett.*, 2010, **10**, 3283.
- 9 M. R. Dirmeyer, J. Martin, G. S. Nolas, A. Sen and J. V. Badding, *Small*, 2009, **5**, 933.
- 10 M. Scheele, N. Oeschler, K. Meier, A. Kornowski, C. Klinke and H. Weller, *Adv. Funct. Mater.*, 2009, **19**, 3476.
- 11 A. Purkayastha, S. Kim, D. D. Gandhi, P. G. Ganesan, T. Borca-Tasciuc and G. Ramanath, *Adv. Mater.*, 2006, **18**, 2958.
- 12 A. Purkayastha, F. Lupo, S. Kim, T. Borca-Tasciuc and G. Ramanath, *Adv. Mater.*, 2006, **18**, 496.
- 13 Y. Deng, Y. Xiang and Y. Song, *Cryst. Growth Des.*, 2009, **9**, 3079.
- 14 T. Wang, R. Mehta, C. Karthik, P. G. Ganesan, B. Singh, W. Jiang, N. Ravishankar, T. Borca-Tasciuc and G. Ramanath, *J. Phys. Chem. C*, 2010, **114**, 1796.
- 15 J. L. Mi, N. Lock, T. Sun, M. Christensen, M. Søndergaard, P. Hald, H. H. Hng, J. Ma and B. B. Iversen, *ACS Nano*, 2010, **4**, 2523.
- 16 W. Lu, Y. Ding, Y. Chen, Z. L. Wang and J. Fang, *J. Am. Chem. Soc.*, 2005, **127**, 10112.
- 17 D. L. Medlin and G. J. Snyder, *Curr. Opin. Colloid Interface Sci.*, 2009, **14**, 226.
- 18 B. A. Cook, M. J. Kramer, X. Wei and J. L. Harringa, *J. Appl. Phys.*, 2007, **101**, 053715.
- 19 T. Matsuo and H. Suzuki, *J. Phys. Soc. Jpn.*, 1977, **43**, 1974.
- 20 I. M. Fishman, G. S. Kino and X. D. Wu, *Phys. Rev. B: Condens. Matter Mater. Phys.*, 1994, **50**, 7192.
- 21 A. Maiti, G. D. Mahan and S. T. Pantelides, *Solid State Commun.*, 1997, **102**, 517.
- 22 A. Bagri, S. P. Kim, R. S. Ruoff and V. B. Shenoy, *Nano Lett.*, 2011, **11**, 3917.
- 23 L. Lu, Y. Shen, X. Chen, L. Qian and K. Lu, *Science*, 2004, **304**, 422.
- 24 Y. T. Zhu, X. Z. Liao and X. L. Wu, *Prog. Mater. Sci.*, 2012, **57**, 1.
- 25 O. Anderoglu, A. Misra, H. Wang, F. Ronning, M. F. Hundley and X. Zhang, *Appl. Phys. Lett.*, 2008, **93**, 083108.
- 26 Y. Q. Cao, X. B. Zhao, T. J. Zhu, X. B. Zhang and J. P. Tu, *Appl. Phys. Lett.*, 2008, **92**, 143106.
- 27 C. S. Lue and Y. K. Kuo, *Phys. Rev. B: Condens. Matter Mater. Phys.*, 2002, **66**, 085121.

- 28 C. S. Lue and Y. K. Kuo, *J. Phys.: Condens. Matter*, 2003, **15**, 877.
- 29 D. G. Cahill, *Rev. Sci. Instrum.*, 1990, **61**, 802.
- 30 T. Yamane, N. Nagai, S. Katayama and M. Todoki, *J. Appl. Phys.*, 2002, **91**, 9772.
- 31 D. M. Rowe, *CRC Handbook of Thermoelectrics: Macro to Nano*, CRC Press/Taylor & Francis, Boca Raton, 2006.
- 32 J. A. Thornton, *J. Vac. Sci. Technol.*, 1974, **11**, 666.
- 33 H. C. Chang and C. H. Chen, *CrystEngComm*, 2011, **13**, 5956.
- 34 M. H. Francombe, *Philos. Mag.*, 1964, **10**, 989.
- 35 F. Besse, C. Boulanger, B. Bolle and J. J. Heizmann, *Scr. Mater.*, 2006, **54**, 1111.
- 36 Z. L. Wang, *J. Phys. Chem. B*, 2000, **104**, 1153.
- 37 V. Russo, A. Bailini, M. Zamboni, M. Passoni, C. Conti, C. S. Casari, A. L. Bassi and C. E. Bottani, *J. Raman Spectrosc.*, 2008, **39**, 205.
- 38 A. Bailini, F. Donati, M. Zamboni, V. Russo, M. Passoni, C. S. Casari, A. L. Bassi and C. E. Bottani, *Appl. Surf. Sci.*, 2007, **254**, 1249.
- 39 K. Lu, L. Lu and S. Suresh, *Science*, 2009, **324**, 349.
- 40 D. L. Medlin, Q. M. Ramasse, C. D. Spataru and N. Y. C. Yang, *J. Appl. Phys.*, 2010, **108**, 043517.
- 41 H. Noro, K. Sato and H. Kagechika, *J. Appl. Phys.*, 1993, **73**, 1252.
- 42 Z. Starý, J. Horák, M. Stordeur and M. Stölzer, *J. Phys. Chem. Solids*, 1988, **49**, 29.
- 43 J. Horák, K. Čermák and L. Koudelka, *J. Phys. Chem. Solids*, 1986, **47**, 805.
- 44 Y. Lan, B. Poudel, Y. Ma, D. Wang, M. S. Dresselhaus, G. Chen and Z. Ren, *Nano Lett.*, 2009, **9**, 1419.
- 45 Y. Zhao, J. S. Dyck, B. M. Hernandez and C. Burda, *J. Am. Chem. Soc.*, 2010, **132**, 4982.
- 46 C. Schumacher, K. G. Reinsberg, R. Rostek, L. Akinsinde, S. Baessler, S. Zastrow, G. Rampelberg, P. Woias, C. Detavernier, J. A. C. Broekaert, J. Bachmann and K. Nielsch, *Adv. Energy Mater.*, 2012, 1.
- 47 A. Mzerd, F. Tcheliobou, A. Sackda and A. Boyer, *Sens. Actuators, A*, 1995, **46–47**, 387.
- 48 C. N. Liao and L. C. Wu, *Appl. Phys. Lett.*, 2009, **95**, 052112.
- 49 M. Scheele, N. Oeschler, I. Veremchuk, K. G. Reinsberg, A. M. Kreuziger, A. Kornowski, J. Broekaert, C. Klinke and H. Weller, *ACS Nano*, 2010, **7**, 4283.
- 50 C. N. Liao, X. W. Su, K. M. Liou and H. S. Chu, *Thin Solid Films*, 2011, **519**, 4394.
- 51 M. V. Kovalenko, B. Spokoyny, J. S. Lee, M. Scheele, A. Weber, S. Perera, D. Landry and D. V. Talapin, *J. Am. Chem. Soc.*, 2010, **132**, 6686.
- 52 H. W. Jeon, H. P. Ha, D. B. Hyun and J. D. Shim, *J. Phys. Chem. Solids*, 1991, **52**, 579.